RESEARCH ARTICLE

Key Points:
- Shallow creep is pervasive along the southernmost 50 km of the San Andreas Fault
- Creep is localized only along transpressional fault segments
- In transtensional areas, creep is distributed over a 1–2 km wide fault zone

Localized and distributed creep along the southern San Andreas Fault

Eric O. Lindsey[1], Yuri Fialko[1], Yehuda Bock[1], David T. Sandwell[1], and Roger Bilham[2]

[1]Institute of Geophysics and Planetary Physics, Scripps Institution of Oceanography, University of California San Diego, La Jolla, California, USA, [2]Department of Geological Sciences, University of Colorado Boulder, Boulder, Colorado, USA

Abstract We investigate the spatial pattern of surface creep and off-fault deformation along the southern segment of the San Andreas Fault using a combination of multiple interferometric synthetic aperture radar viewing geometries and survey-mode GPS occupations of a dense array crossing the fault. Radar observations from Envisat during the period 2003–2010 were used to separate the pattern of horizontal and vertical motion, providing a high-resolution image of uplift and shallow creep along the fault trace. The data reveal pervasive shallow creep along the southernmost 50 km of the fault. Creep is localized on a well-defined fault trace only in the Mecca Hills and Durmid Hill areas, while elsewhere creep appears to be distributed over a 1–2 km wide zone surrounding the fault. The degree of strain localization is correlated with variations in the local fault strike. Using a two-dimensional boundary element model, we show that stresses resulting from slip on a curved fault can promote or inhibit inelastic failure within the fault zone in a pattern matching the observations. The occurrence of shallow, localized interseismic fault creep within mature fault zones may thus be partly controlled by the local fault geometry and normal stress, with implications for models of fault zone evolution, shallow coseismic slip deficit, and geologic estimates of long-term slip rates.

1. Introduction

Laboratory studies of rock friction suggest that rocks exhibit velocity-strengthening behavior at low temperature and normal stress [*Dieterich*, 1978; *Marone et al.*, 1991; *Blanpied et al.*, 1995], implying that the shallow part of active faults should undergo stable sliding, or creep, in the interseismic period. This prediction is reinforced by numerical models of faults governed by rate-state friction, which show stable sliding at low normal stress even if friction is not velocity-strengthening [*Tse and Rice*, 1986; *Marone and Scholz*, 1988; *Scholz*, 1998; *Lapusta et al.*, 2000; *Kaneko et al.*, 2013]. Shallow interseismic creep is indeed observed on a number of seismically active faults, for example, the Rodgers Creek Fault [*Funning et al.*, 2007], Hayward Fault [*Savage and Lisowski*, 1993; *Bürgmann et al.*, 2000a], Imperial Fault [*Lyons et al.*, 2002; *Crowell et al.*, 2013], and Superstition Hills Fault [*Wei et al.*, 2009, 2013] in California, and part of the North Anatolian Fault in Turkey [*Ambraseys*, 1970; *Cakir et al.*, 2005; *Kaneko et al.*, 2013]. Other faults creep throughout the entire seismogenic layer, such as the San Andreas Fault (SAF) north of Parkfield [e.g., *Titus et al.*, 2005; *Tong et al.*, 2013] and part of the Haiyuan Fault in China [*Jolivet et al.*, 2013].

Such behavior, however, may not be typical, as many other faults do not undergo interseismic creep at the surface, for example, most of the SAF between Parkfield and San Gorgonio [*Genrich and Bock*, 1992; *Tong et al.*, 2013] and the San Jacinto Fault [*Louie et al.*, 1985; *Lindsey et al.*, 2013], most of the North Anatolian Fault [*Cakir et al.*, 2005], and the Altyn Tagh Fault in Tibet [*Elliott et al.*, 2008]. Because the accumulation of potential seismic moment may be significantly reduced by the occurrence of shallow creep, the latter plays an important role in our understanding of fault mechanics and earthquake hazard.

A related question is the nature of deformation within active fault zones. Evidence of significant off-fault damage and distributed deformation extending from a few tens of meters to a few kilometers has been documented by geologic [e.g., *Rockwell et al.*, 2002; *Dor et al.*, 2006; *Faulkner et al.*, 2006; *Oskin et al.*, 2007; *Wechsler et al.*, 2009; *Shelef and Oskin*, 2010; *Titus et al.*, 2011], seismic [e.g., *Spudich and Olsen*, 2001; *Ben-Zion et al.*, 2003; *Lewis et al.*, 2005; *Cochran et al.*, 2009], and geodetic [e.g., *Fialko et al.*, 2002; *Jolivet et al.*, 2009; *Cakir et al.*, 2012] observations. Models of seismic rupture in an elastoplastic domain suggest that dynamic stresses can trigger distributed coseismic yielding near the fault in a pattern that progressively widens toward the surface [*Kaneko and Fialko*, 2011], reminiscent of geologically observed flower structures

[e.g., *Sylvester*, 1988]. Field and geodetic evidence suggests that this type of inelastic deformation may be partly responsible for the shallow slip deficit observed during major earthquakes [*Fialko et al.*, 2005], possibly resulting in an inverse correlation between the degree of shallow slip deficit and fault maturity [*Dolan and Haravitch*, 2014].

In this study, we investigate near-field deformation along the southern section of the SAF, a mature strike-slip fault that is in the late interseismic phase of the earthquake cycle [*Sieh and Williams*, 1990; *Fialko*, 2006; *Lundgren et al.*, 2009; *Lindsey and Fialko*, 2013]. Parts of the southern section of the SAF are known to creep near the surface; *Sieh and Williams* [1990] estimated an average creep rate of 2–4 mm/yr since the last major earthquake ∼300 years ago. Data from creepmeters near Durmid Hill show that the shallow creep is not entirely steady [*Bilham et al.*, 2004], and triggered slip of up to several centimeters has been observed following nearby large (*M*6+) earthquakes [*Allen et al.*, 1972; *Sieh*, 1982; *Rymer*, 2000; *Rymer et al.*, 2002; *Wei et al.*, 2011]. Previous interferometric synthetic aperture radar (InSAR) observations of this area have confirmed the occurrence of creep, although the inferred creep rates varied widely, possibly due to unaccounted differential vertical motion across the fault zone [*Lyons and Sandwell*, 2003; *Fialko*, 2006; *Wei et al.*, 2011; *Manzo et al.*, 2011; *Tong et al.*, 2013]. However, none of the studies identified continuous creep along the entire fault segment except during the Landers earthquake, when it was observed by InSAR [*Lyons and Sandwell*, 2003] but not in the field [*Rymer*, 2000]. Clear evidence of nontriggered surface offsets has been confined to the Durmid Hill and Mecca Hills areas, two approximately 12 km long segments where the local fault strike leads to transpression and locally elevated topography [*Bilham and Williams*, 1985]. In the intervening areas, *Bilham and Williams* [1985] noted a poor expression of the fault trace and lack of localized creep.

We present new geodetic observations of the pattern of shallow creep on the southern section of the SAF and show that creep occurs along the entire fault section, but with varying degrees of localization. Using a combination of ascending and descending InSAR observations from Envisat and survey-mode occupations of a dense array of Global Positioning System (GPS) monuments, we determine the average rate of shear near the fault trace. The use of multiple InSAR viewing geometries allows us to isolate and remove the effects of vertical motion that has limited previous InSAR studies of the area [*Lyons and Sandwell*, 2003; *Wei et al.*, 2011; *Manzo et al.*, 2011]. The improved data set allows us to estimate the creep rate and width of the deforming fault zone. We show that the degree of strain localization strongly correlates with the fault geometry and propose that this pattern is ultimately controlled by the fault-normal stress.

2. Observations

2.1. InSAR Data

InSAR is well suited to image shallow interseismic fault creep [e.g., *Bürgmann et al.*, 2000b; *Cakir et al.*, 2005; *Jolivet et al.*, 2012; *Kaneko et al.*, 2013; *Shirzaei and Bürgmann*, 2013]. The main limitations of InSAR for this purpose are short-wavelength noise from atmospheric variability, and possible contamination of the signal by vertical motions of the ground, to which the radar viewing geometry makes InSAR particularly sensitive. Typically, atmospheric noise is reduced by means of temporal averaging or stacking [*Peltzer et al.*, 2001; *Fialko*, 2006], or other forms of smoothing or filtering [e.g., *Berardino et al.*, 2002; *Shirzaei and Walter*, 2011; *Hetland et al.*, 2012]. We adopted a stacking method that identifies and preferentially includes radar scenes with the least atmospheric noise, resulting in a better signal-to-noise ratio with a smaller set of interferograms. We take advantage of different radar viewing geometries (corresponding to the ascending and descending satellite orbits) to separate horizontal and vertical motions provided the horizontal direction of motion is known.

We processed all available SAR data from Envisat descending track 356 (frames 2925–2943) and ascending track 77 (frames 657–675), which span the southernmost segment of the SAF from Bombay Beach to Indio, California. There were 46 usable radar acquisitions for track 356 and 45 acquisitions for track 77 spanning the period 2003–2010. The raw data were processed using the open-source software GMTSAR [*Sandwell et al.*, 2011]; interferograms were unwrapped using the SNAPHU algorithm [*Chen and Zebker*, 2000].

We initially generated a complete set of interferograms satisfying certain baseline criteria for each track (141 and 135 for tracks 356 and 77, respectively). To minimize the contribution of atmospheric noise to the estimated velocities, we adopted a common-point stacking method to identify and exclude scenes with the largest noise from the final stack [*Fialko and Tymofyeyeva*, 2013]. Some scenes did not have enough
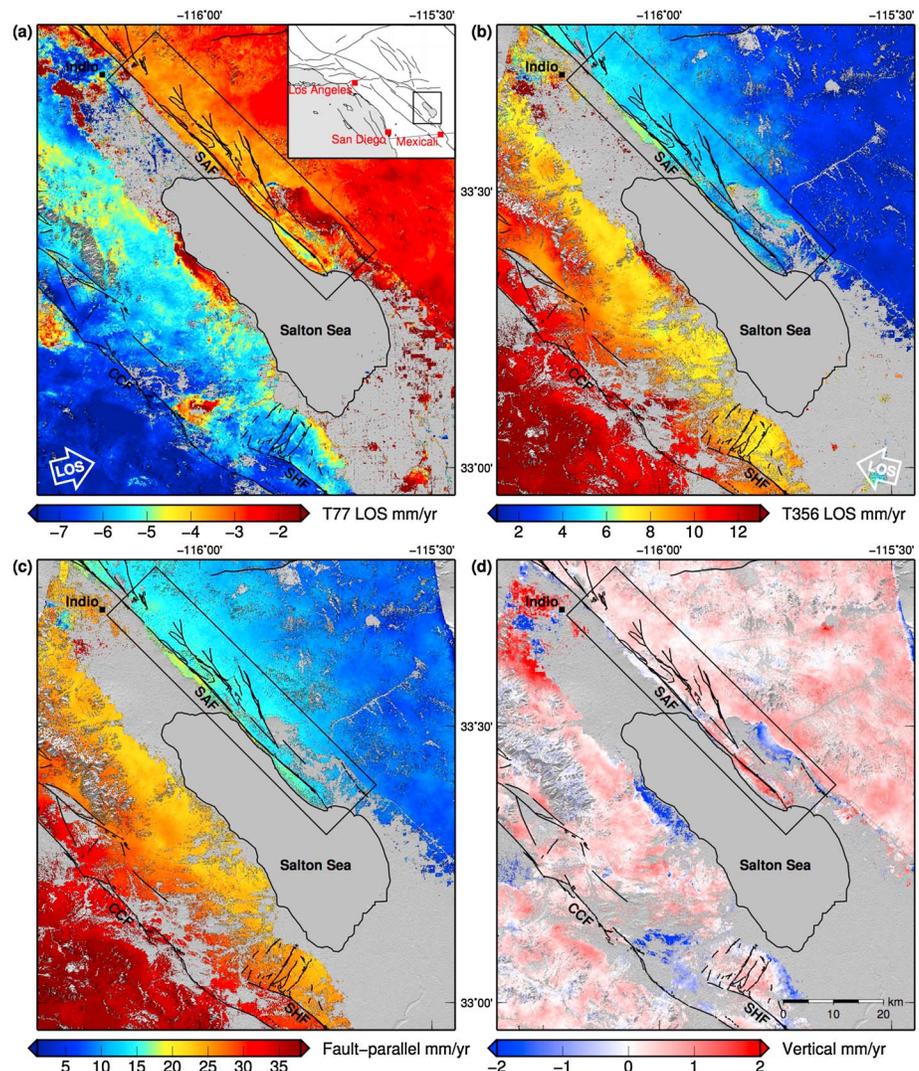
Figure 1. Ground velocities inferred from Envisat InSAR observations. (a) Track 77 average line of sight (LOS) veloci-ties. (b) Track 356 LOS velocities. (c) Fault-parallel velocities (azimuth 315.8°) and (d) vertical velocities, computed from Figures 1a and 1b using equation (2). Labels denote the San Andreas Fault (SAF), Superstition Hills Fault (SHF), and Coyote Creek Fault (CCF). Rectangular box indicates area shown in Figure 2. Faults shown in black are from the U.S. Geological Survey (USGS) Quaternary fault and fold database (available http://earthquake.usgs.gov/hazards/qfaults/). All figures were prepared using the Generic Mapping Tools software package [*Wessel et al.*, 2013].

connecting interferograms or were too decorrelated to provide a reliable estimate of the atmospheric noise, and were therefore excluded from the data set. Finally, we selected a subset of interferograms which prefer-entially connect the scenes with the lowest inferred atmospheric noise, did not contain unwrapping errors, and maintained good correlation along the SAF (29 and 27 interferograms for tracks 356 and 77, respec-tively). We found that the results varied minimally with the selection of different subsets of interferograms connecting scenes with the lowest atmospheric noise. Estimated atmospheric noise levels along with the initial and final interferogram sets are shown in supporting information Figure S1.

We removed potential long-wavelength orbital and atmospheric artifacts from each data set by combin-ing the stacks with continuous GPS data using the sum-remove-filter-restore (SURF) approach [*Tong et al.*, 2013]. Horizontal GPS velocities with uncertainties less than 0.5 mm/yr [*Shen et al.*, 2011] were interpo-lated using a bicubic spline and subtracted from the average line of sight (LOS) velocities for each track. The results were high-pass filtered with a two-dimensional Gaussian filter at a 40 km cutoff wavelength and added back to the long-wavelength interpolated GPS map. The final LOS velocities are shown in Figures 1a
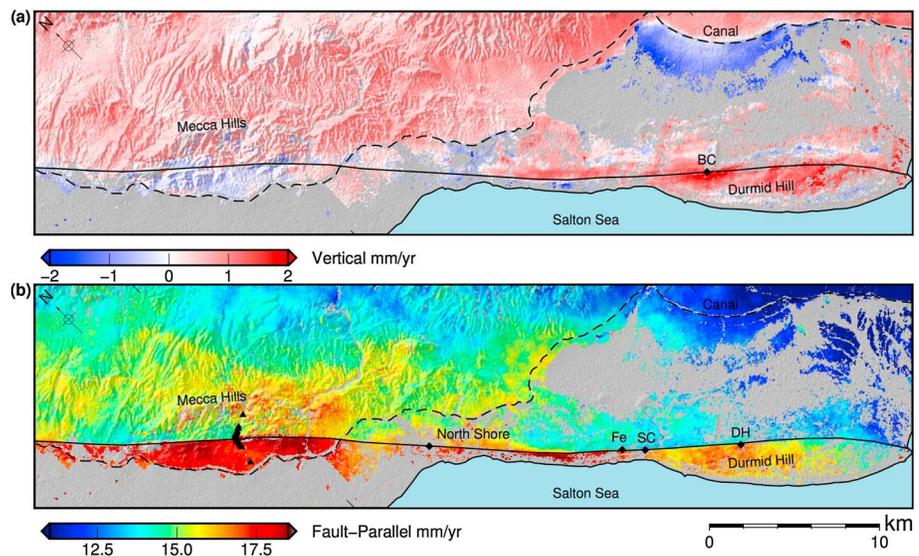
Figure 2. Zoom of boxed region in Figure 1: (a) Vertical ground velocity inferred from Envisat InSAR observations. BC denotes location of Bat Caves Buttes leveling line [*Sylvester et al.*, 1993]. (b) Inferred fault-parallel (azimuth 315.8°) ground velocity. Black line denotes trace of the SAF. Diamonds indicate locations of creepmeters at: North Shore, Ferrum (Fe), Salt Creek (SC), and Durmid Hill (DH). Triangles indicate locations of GPS monuments at Painted Canyon. Dashed line indicates location of the Coachella Canal.

and 1b and retain the short-wavelength information provided by InSAR but agree with the GPS at wavelengths longer than 40 km. The results contain some residual short-wavelength noise, for example, faster velocities in the Mecca Hills to the NE of the SAF, which may be caused by atmospheric delays correlated with topography.

Because of the radar viewing geometry, Envisat observations are $\sim$ 2.7 times more sensitive to vertical motion than to SAF-parallel motion of the ground. In areas such as the Coachella valley where aquifer-related vertical deformation is significant [e.g., *Lyons and Sandwell*, 2003], this signal can overwhelm the small horizontal motions associated with fault creep. By combining observations from two independent look directions, we are able to project the information onto any desired set of two orthogonal basis vectors, assuming the third component is zero [e.g., *Fialko et al.*, 2002]. In the study region, GPS data suggest that the long-term deformation is essentially simple shear parallel to the fault [*Shen et al.*, 2011]. Therefore, given satellite look vectors with Cartesian components (e_i, n_i, u_i), the observed LOS velocities v_i may be projected onto the fault-parallel and vertical directions (v_f, v_z) as follows:

$$\mathbf{P} = \begin{pmatrix} e_1 \sin\alpha + n_1 \cos\alpha & u_1 \\ e_2 \sin\alpha + n_2 \cos\alpha & u_2 \end{pmatrix} \tag{1}$$

$$\begin{pmatrix} v_f \\ v_z \end{pmatrix} = \mathbf{P}^{-1} \begin{pmatrix} v_1 \\ v_2 \end{pmatrix}, \tag{2}$$

where α is the mean strike of the SAF in the study region (315.8°). The results of this decomposition are shown in Figures 1c and 1d, and the area close to the SAF is shown in more detail in Figure 2. The relationship is exact in the case of a constant deformation rate and negligible fault-perpendicular motion. Regional GPS velocities [*Shen et al.*, 2011] and our own GPS results (see below) confirm that the motion near the SAF is essentially fault parallel, although there may be a slight (<1 mm/yr) fault-perpendicular translation of the region. This translation will be reflected in the inferred fault-parallel velocities as a long-wavelength offset that does not affect the observed rate or pattern of fault creep. Smaller-scale fault-perpendicular motion close to the fault such as dip-slip motion could alter the fault-parallel velocities in a manner that would affect creep observations. However, this behavior is not evident in the GPS observations presented below, and significant vertical offsets indicative of dip slip have not been observed during triggered creep events along the SAF [*Rymer*, 2000; *Rymer et al.*, 2002].

GPS time series from the Scripps Orbit and Permanent Array Center (http://sopac.ucsd.edu) suggest that time-dependent or seasonal signals during the Envisat observation period typically have an amplitude <1 mm/yr. Where a larger time-dependent vertical signal is present, some contamination of the horizontal velocity field is visible, for example, the area southwest of Indio in Figure 1c. Closer to the SAF, these artifacts appear to be small and should not affect the inferred spatial pattern of fault creep. To verify these assumptions, we compare the InSAR velocities with several independent ground-based observations of the rates of uplift and creep along the fault.

2.2. Vertical Motion and Uplift of Durmid Hill

Vertical velocities near the SAF trace are shown in detail in Figure 2a. A broad pattern of subsidence to the northwest of the fault appears to coincide with the Coachella Canal Lining Project, which replaced a 59 km segment of unlined canal (dashed line in Figure 2a) by a cement-lined canal in 2006, conserving an estimated 26,000 acre-feet of water per year (San Diego County Water authority, 2014, available at http://www.sdcwa.org/canal-lining-projects). Conservation of this water, which previously entered the groundwater system along the unlined section of the canal, may have resulted in the observed long-term subsidence of approximately 1–2 mm/yr. A similar subsidence pattern in ERS data (1993–1999) was described by *Lyons and Sandwell* [2003], though they noted this may have been related to excess extraction of the groundwater for local use. Smaller, localized areas of subsidence elsewhere in the image may likewise be related to water pumping. Comparison of time-series observations of this subsidence with hydrologic data (e.g., well extraction rates) would make an interesting subject for future work.

The near-fault pattern of uplift along Durmid Hill, on the other hand, appears to be tectonic in origin. Here the InSAR velocities indicate uplift at a rate of 1.5–2 mm/yr, centered just southwest of the fault trace (Figure 3), in good agreement with geologic estimates of the long-term rate of uplift of Durmid Hill over the past 10^4–10^6 years [*Bürgmann*, 1991] and with the results of a leveling line across the fault at this location [*Sylvester et al.*, 1993]. The observed 8:1 ratio of horizontal offset to vertical uplift at Salt Creek [*Bilham and Williams*, 1985; *Sylvester et al.*, 1993] suggests a long-term fault slip rate of 12–20 mm/yr, consistent with recent geodetic and geologic results [*van der Woerd et al.*, 2006; *Fialko*, 2006; *Lundgren et al.*, 2009; *Lindsey and Fialko*, 2013]. A good agreement between geologic and geodetic estimates of vertical velocities suggests that the uplift of Durmid Hill occurs primarily in the interseismic period, rather than during large earthquakes.

2.3. GPS and Creepmeter Data

The mean LOS velocities ignore the possible time-dependence of shallow creep along the fault, so the results may be sensitive to the time span of the particular interferograms used in the stacks. To verify that the inferred fault-parallel velocities are representative of the secular rates, we compare the InSAR data with the results of GPS occupations of a dense array of monuments at Painted Canyon along the Mecca Hills segment, as well as with several creepmeters along the Durmid Hill and North Shore segments.

The Painted Canyon GPS array consists of 34 closely spaced monuments, the surviving elements of a leveling line installed in 1985 [*Sylvester et al.*, 1993]. Locations are shown in Figure 2b. The monuments were reoccupied with GPS 4 times between 2007 and 2014. The first three surveys consisted of short occupations ranging from 15 to 60 min, repeated twice for each station. This rapid-static method is justified by analyses of strong temporal correlations in GPS time series which suggest that two short occupations separated by several hours may be as accurate as a single occupation of moderate length [*Bock et al.*, 2000]. The final survey consisted of 6–10 h occupations for each site. Data were processed using the Real Time Dynamics software package [*Genrich and Bock*, 2006]. For each site with at least three observations, we fit a line to the horizontal components of the site motion relative to nearby continuous site CACT, which was used to provide the local reference velocity in the North America Fixed (NAFD) reference frame [*Shen et al.*, 2011]. Marker positions and velocities are listed in supporting information Table S1. The results are shown in Figure 4. The average fault-parallel GPS velocities compare favorably with InSAR data obtained at the same location over a different time interval, suggesting that possible time dependence of the signal does not significantly bias these observations. Additionally, the GPS data show that at this location, creep is localized in a slip zone that is narrower than the 35 m spacing between the nearest monuments on either side of the fault trace.

Fault-perpendicular GPS velocities are plotted in Figure 4b. There is a small (0.5–1 mm/yr) net south-westward translation of the array relative to the fault trace. This motion is also seen to some extent
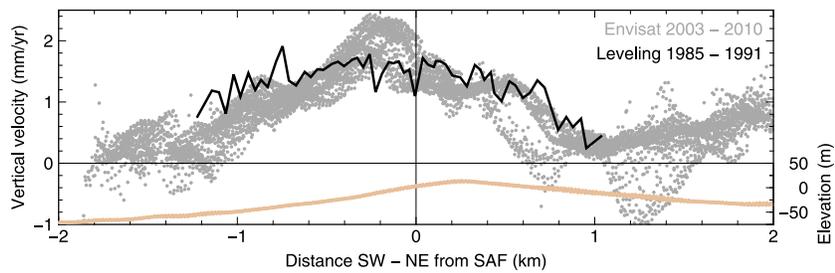
Figure 3. Vertical uplift across Durmid Hill at Bat Caves Buttes, inferred from InSAR (gray) and from a leveling line (black) at the same location [*Sylvester et al.*, 1993]. Topographic profile is shown in tan. Note the apparent asymmetry of uplift with respect to both the fault trace (vertical line) and the topographic profile.

in Figure 10 of *Shen et al.* [2011] and may represent long-wavelength compression across the region or a small net translation of the GPS network that is a result of the NAFD reference frame definition. In either case, the data do not suggest significant interseismic compression across the fault zone, suggesting that the assumption of no fault-perpendicular motion in the InSAR processing does not bias the creep observations.

We also compare the InSAR-derived velocities with the rates recorded by creepmeters installed in four locations along the fault and operated by the University of Colorado Boulder [*Bilham et al.*, 2004] (available at http://cires.colorado.edu/~bilham/creepmeter.file/creepmeters.htm). The rates observed at the Durmid Hill, Salt Creek, and Ferrum instruments are summarized in Figures 5a–5c (locations shown in Figure 2b) and show good agreement with the InSAR data at the same locations. The instrument at North Shore (Figure 5d) has recorded no detectable creep across its 10 m span, consistent with the lack of a discontinuity in the InSAR velocity field. However, the InSAR suggests that in this area, significant deformation is taking place over a zone approximately 1.5 km wide.

2.4. Rate and Degree of Localization of Shallow Creep
Fault-parallel velocities for the area surrounding the SAF are shown in detail in Figure 2b. Surface creep is visible along much of the SAF from Bombay Beach to Indio, California. In some areas creep is highly
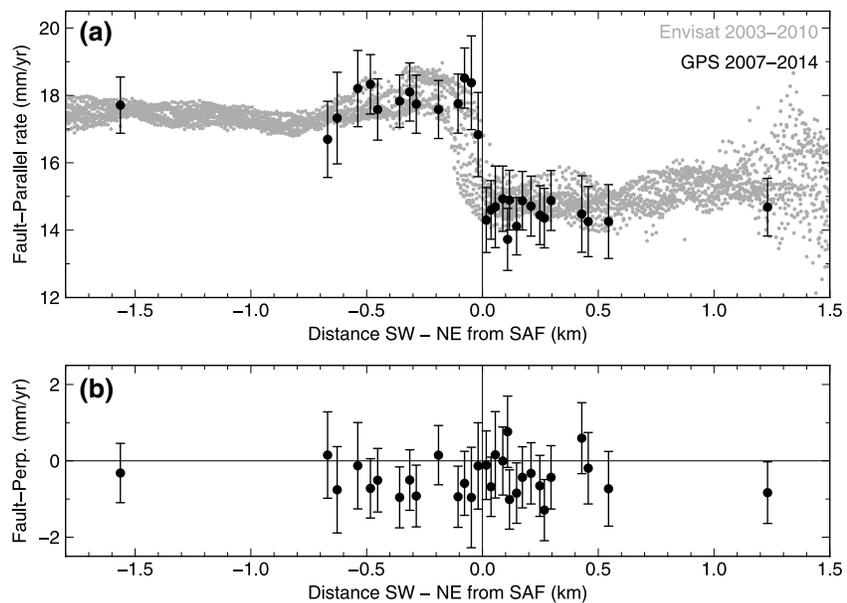
Figure 4. (a) Comparison of Envisat-derived fault-parallel velocities with GPS velocities at Painted Canyon. (b) Fault-perpendicular GPS velocities; note that overall westward translation is related to the reference frame definition. GPS monument locations are shown in Figure 2b; locations and velocities are listed in supporting information Table S1.
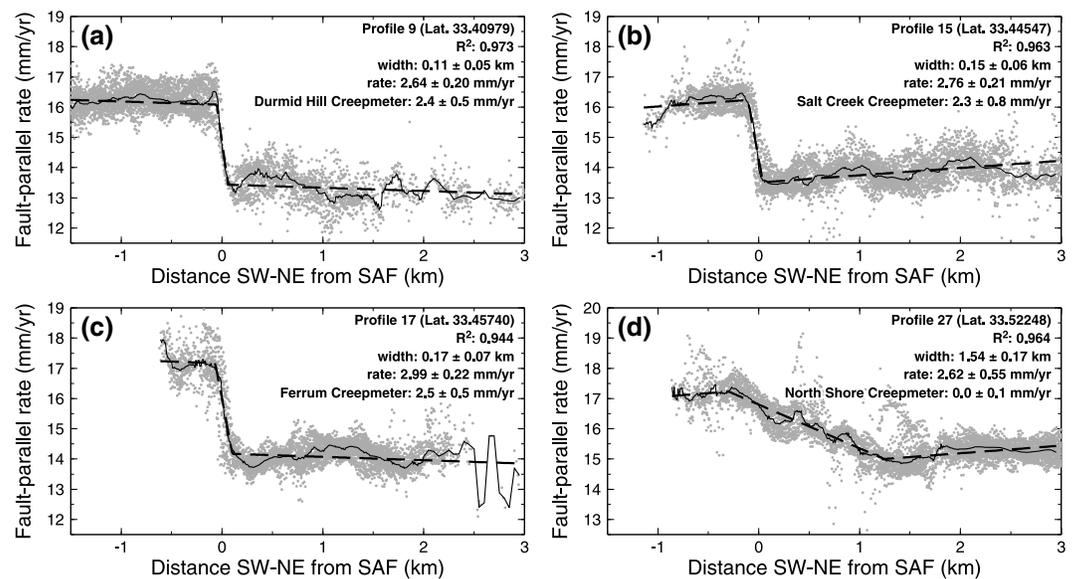
Figure 5. Profiles showing Envisat-derived fault-parallel velocities (gray) resampled via a median filter to uniform spacing (black curve) and best-fitting 3-piece linear model (black dashed line). Locations correspond to the (a) Durmid Hill, (b) Salt Creek, (c) Ferrum, and (d) North Shore creepmeters, shown as diamonds in Figure 2b. The full set of 52 across-fault profiles is shown in supporting information Figure S2.

localized, for example, at Durmid Hill and the Mecca Hills, while in others it appears to be distributed across a finite zone, for example, along the segment passing through the town of North Shore.

Previously, creep within the Mecca Hills was identified in the field only intermittently along the fault [*Allen et al.*, 1972; *Sieh*, 1982; *Rymer*, 2000; *Rymer et al.*, 2002], primarily north of Painted Canyon. The InSAR reveals that creep is continuous along this segment, but to the south of Painted Canyon the creep is offset 200–300 m northeast of the main SAF trace in the USGS Quaternary fault and fold database (available at http://earthquake.usgs.gov/hazards/qfaults/). Here the creep coincides with the surface trace of the Skeleton Canyon Fault, a minor structure associated with transpression within the Mecca Hills and not previously inferred to accommodate significant lateral motion [*McNabb and Dorsey*, 2012].

To estimate the rate of creep along the fault and the width of the shear zone, we used a maximum likelihood approach [*Neal*, 2003; *Tarantola*, 2005]. We selected data within 1 km wide, 10 km long profiles drawn perpendicular to the local fault strike every 1 km along the fault between 33.35°N and 33.68°N, resulting in a total of 52 profiles. Because of variable radar correlation along the fault, the density of data may be highly nonuniform across a given profile. To improve the robustness of the fits in these cases, we applied a median filter to each profile with a width of 200 m. In combination with spatial filtering applied during the InSAR processing, this procedure limits our ability to resolve the width of the creeping zone where it is less than 200 m, for example, along the Durmid and Mecca Hills segments. The filter does not affect the results where the zone is wider than 200 m, as confirmed by experiments using several filter sizes.

We then fit a three-piece linear function to the observed velocities, with the offsets between the two corners used to determine the creep rate and shear zone width at each location. Residual atmospheric noise present in the InSAR at 1–10 km wavelengths, or possibly variations in the depth extent of the creep, may introduce a velocity gradient across the fault, requiring an additional parameter (slope) to fit the data outside the fault zone. We require that this slope is equal on both sides of the fault to avoid overparametrizing the model. The model requires five parameters in total; we used a Markov Chain Monte Carlo sampling method [*Neal*, 2003; *Lindsey and Fialko*, 2013] to find the best-fitting parameters and their uncertainties, assuming the L_2 norm (sum of squared residuals) for the misfit function.

Selected profiles corresponding to the locations of the four creepmeters are shown in Figure 5; fits to all profiles are shown in supporting information Figure S2. The best-fitting creep rate and shear zone width from all profiles are summarized in Figures 6a and 6b, with 1 sigma uncertainties shown in gray. The results indicate
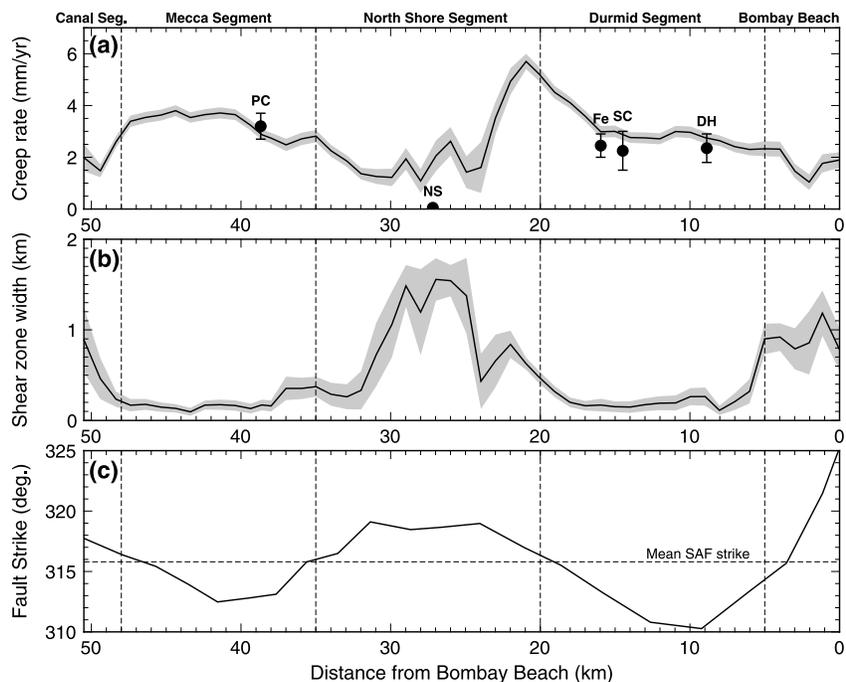
Figure 6. (a) Estimated creep rate from InSAR, with 1 sigma uncertainties (gray) and GPS/creepmeter creep rates for comparison (black dots). Labels indicate Painted Canyon GPS array (PC); North Shore (NS), Ferrum (Fe), Salt Creek (SC), and Durmid Hill (DH) creepmeters. (b) Estimated shear zone width for 1 km wide profiles drawn across the fault. (c) Local fault strike relative to North, estimated every 2 km using fault trace shown in Figure 2. Segment boundaries as identified by *Bilham and Williams* [1985] are denoted by dashed lines.

that the creep rate is nonzero everywhere along the fault. Creep is highly localized along the Durmid and Mecca Hills segments, while in other areas it is distributed across a 1–2 km wide zone. Note that although a broad fault zone consisting of damaged material and multiple slip surfaces (or "flower structure") has been observed in the Mecca Hills [*Sylvester*, 1988] and is suggested at Durmid hill by the pattern of ongoing uplift (Figure 2a), the existence of such a structure does not appear to cause distributed creep during the inter-seismic period, and it appears that among the many slip surfaces identified in the Mecca Hills, only one is active at a given time. The inferred creep rate varies from a minimum of 1–2 mm/yr along the North Shore segment to a maximum of 6 mm/yr just to the south of this segment. Figure 6c shows the local fault strike, with segment boundaries defined by *Bilham and Williams* [1985]. There is an apparent correlation between the width of the creeping zone and the local fault strike, with segments trending more westerly having more localized surface creep than those trending more northerly.

3. Coulomb Stressing Rates on a Nonplanar Fault

To understand how small variations in the fault strike may lead to significant variations in the pattern of deformation within the fault zone, we modeled the evolution of stresses near a curved fault using the two-dimensional boundary element model (BEM) TWODD [*Crouch and Starfield*, 1983; *Fialko and Rubin*, 1997]. The model is quasistatic and assumes constant fault friction governed by the Mohr-Coulomb criterion $\tau = \sigma\mu$ in an otherwise perfectly elastic material. Deformation is plane strain (all vertical components of strain are zero) and slip on the fault is driven by the application of initially uniform principal stresses σ_1 and σ_3. Slip is computed iteratively until all fault elements satisfy the Mohr-Coulomb slip criterion.

For a homogeneous, unfaulted material with cohesion c and friction angle $\phi = \tan^{-1}\mu$, the Mohr-Coulomb yield criterion on an optimally oriented plane is reached when the maximum shear stress $\frac{1}{2}(\sigma_1 - \sigma_3)$ exceeds a threshold

$$\frac{1}{2}(\sigma_1 - \sigma_3) \geq \frac{1}{2}(\sigma_1 + \sigma_3)\sin\phi + c\cos\phi. \qquad (3)$$
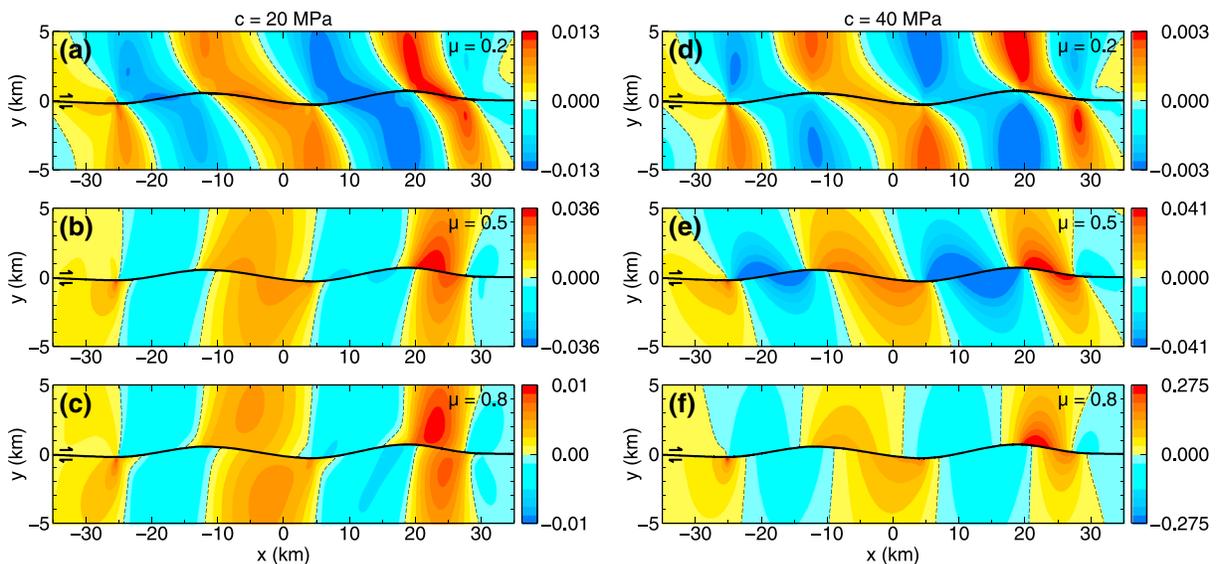
Figure 7. Change in Mohr-Coulomb failure ratio Δr (equation 5) due to a far-field shear stress increment $\Delta\sigma_{xy} = 10$ kPa and resulting slip on the fault (solid black line). The fault has a constant coefficient of friction μ specified in each panel. Material cohesion is (a–c) 20 MPa and (d–f) 40 MPa.

For a given state of stress, we may therefore define the "closeness to failure" ratio

$$r(\sigma) = \frac{\sigma_1 - \sigma_3}{(\sigma_1 + \sigma_3)\sin\phi + 2c\cos\phi}, \quad (4)$$

which reaches 1 when the material begins to yield. Because the absolute stress conditions in the Earth are not known, we are interested in the rate of change of r, given by the time derivative of (4). For modeling purposes, we approximate this derivative by a discrete increment Δr computed as the total change in r due to a stress increment $\Delta\sigma = \sigma' - \sigma$:

$$\Delta r = r(\sigma') - r(\sigma). \quad (5)$$

Areas where $\Delta r > 0$ are being brought closer to Mohr-Coulomb failure, while areas with $\Delta r < 0$ move away from failure. Although the absolute magnitude of Δr is sensitive to the assumed stress increment, cohesion, and the coefficient of friction in the material, we find that the sign of Δr is unchanged at a given location for different modeling assumptions as long as the stress increment $\Delta\sigma$ remains small. Note that the BEM formulation does not include true Mohr-Coulomb yielding off the fault plane or the resulting changes in the stress state this would imply. In addition, the occurrence of yielding depends not only on Δr but also on the absolute state of stress in the Earth and the history of the material. Thus, the value of Δr is indicative only of where yielding is most likely to initiate and does not necessarily represent the magnitude or pattern of long-term yielding.

We assume initial stress conditions such that a fault oriented along the mean strike of the SAF (defined as the x axis) is critically stressed, given a friction coefficient μ and a mean compressive stress of -50 MPa. For example when $\mu = 0.5$, we obtain $\sigma_{xx} = -72$ MPa, $\sigma_{yy} = -48$ MPa, and $\sigma_{xy} = 24$ MPa. The plane strain condition implies $\sigma_{zz} = \nu(\sigma_{xx} + \sigma_{yy})$ where Poisson's ratio $\nu = 0.25$, so that $\sigma_{zz} = -30$ MPa, corresponding to approximately 2 km depth. Because the fault is curved, some portions will not be initially critically stressed under these conditions. Therefore, the shear stress σ_{xy} is first increased by 100 kPa to ensure the entire (curved) fault has reached the Mohr-Coulomb criterion and begun to slip. We then apply an additional shear stress increment of 10 kPa and compute Δr according to equation (5).

Figure 7 shows the pattern of Δr for different values of friction μ ranging between 0.2 and 0.8, and cohesion c of 20 and 40 MPa. In all cases Mohr-Coulomb failure is predicted to initiate ($\Delta r > 0$) along transtensional segments of the fault and on the outside corners of fault bends, where the mean compressive stress is reduced by fault slip. These simulations favor an intermediate coefficient of friction ($\mu \sim 0.5$, Figures 7b and 7e) or high coefficient of friction and cohesion (Figure 7f) that give rise to maximum values of Δr on the

fault, rather than several kilometers away (Figures 7a, 7c, and 7d). Note that while the pattern of Δr can be compared between panels in Figure 7, the absolute magnitude of Δr is not necessarily comparable between different sets of modeling assumptions.

4. Discussion

Envisat's multiple radar viewing directions allow us to separate the contributions of vertical and fault-parallel deformation to the signal, resolving an issue that limited previous studies of the region [*Lyons and Sandwell*, 2003; *Manzo et al.*, 2011; *Wei et al.*, 2011; *Tong et al.*, 2013]. While field and creepmeter observations have suggested that shallow fault creep is time-dependent [*Rymer*, 2000; *Rymer et al.*, 2002; *Bilham et al.*, 2004], an overall good agreement between average creep rates derived from InSAR, GPS, creepmeter, and longer-term geologic observations suggests that the 5–10 year averages are representative of the long-term interseismic rates (Figures 4, 5, and 6). The inferred vertical and horizontal velocities across the southern-most SAF suggest a pattern of alternating localized and distributed creep and aseismic uplift (Figure 2). Our results confirm the suggestion of *Bilham and Williams* [1985] that along certain segments the creep may be "distributed over a wide fault zone and has thereby escaped detection."

At low confining pressure, shear failure of brittle materials involves both frictional sliding and tensile (Mode I) microcracking [*Melin*, 1986]. Tensile microcracking is inhibited at higher normal stresses, leading to shear failure (Mode II) and progressive localization over time [e.g., *Petit and Barquins*, 1988; *Lockner et al.*, 1992]. This mechanism may explain the localized nature of creep along segments of the fault experiencing higher compressional stresses, and the lack of localization where normal stress is lower. Assuming the off-fault material follows the Mohr-Coulomb yield criterion, we have devised a simple two-dimensional boundary element model that suggests distributed yielding is most likely to occur along segments of the fault with the lowest fault-normal stress—i.e., where the local stress state is transtensional. Conversely, distributed yielding is inhibited where the stress is transpressional (Figure 7). This model reflects the observed pattern of variations in the shear zone width along strike (Figure 6b), although it does not directly predict the width of the deforming zone.

The model also suggests that the creep rate should be highest along transtensional segments, which is not observed (Figure 6a). The along-strike variations in observed creep rates may instead be indicative of a longer-term accommodation of slip that includes seismic events. For example, if transpressional areas are characterized by enhanced velocity strengthening friction and/or greater depth of the velocity-strengthening to velocity-weakening transition, these areas would be expected to creep at a higher rate during the interseismic period [*Savage and Lisowski*, 1993; *Kaneko et al.*, 2013]. *Sieh and Williams* [1990] suggested that transpressional segments may also be subject to higher-pore fluid pressures, further reducing resistance to aseismic slip. However, additional studies are needed to determine whether along-strike variations in the surface creep rate resulting from these factors could persist over much of the interseismic period (hundreds of years).

Continued slip on a curved fault typically results in straightening and reduced geometric complexity [*Wesnousky*, 1988; *Stirling et al.*, 1996]. In contrast, our model results predict patterns of inelastic failure that may in some cases act to preserve the wavy fault geometry and alternating zones of localized/distributed deformation. In particular, the likelihood of Mohr-Coulomb yielding on the extensional side of fault bends (Figure 7) would favor the exaggeration of these fault bends over time. This tendency is reduced for lower values of the coefficient of friction μ. These observations should be treated with caution, however, as the model does not account for the long-term evolution of stresses resulting from inelastic behavior or from changes in the fault geometry, both of which may significantly modify the pattern of failure. Future work is needed to clarify whether this type of geometric complexity can persist over the long term or is only a transient feature within an evolving system.

In either case, distributed creep of the kind observed here (Figures 2b and 6) may be more ubiquitous than is currently recognized. For example, *Cakir et al.* [2012] found that along parts of the North Anatolian Fault, postseismic creep following the 1999 Izmit earthquake occurs over an approximately 1–2 km wide shear zone. *Hsu and Bürgmann* [2006] found that shallow creep along the Longitudinal Valley Fault in Taiwan produces a similar, several km wide signal in some sections. *Lindsey et al.* [2013] identified an anomalously high strain rate along the Anza segment of the San Jacinto Fault in Southern California and argued that it cannot be fully explained by elastic deformation due to a compliant fault zone, and thus may require inelastic

yielding in the interseismic period. To the best of our knowledge, there is no evidence for a kilometer-wide compliant zone surrounding the southern SAF from seismic tomography [e.g., *Allam and Ben-Zion*, 2012], making elastic deformation an unlikely explanation for the observed pattern of strain (Figure 2b). Even if such a zone were present, it would be unlikely to fully account for the observed strain rates within the fault zone, although further modeling would be necessary to assess the relative contribution of the two effects.

We have thus far not considered variations in the pattern of creep with depth and along strike which could potentially explain the observations without requiring distributed inelastic deformation. There are two possibilities: first, that the segments showing a broad pattern of strain are fully locked and the high strain rate is caused by edge effects from creeping sections of the fault to the north and south, and second, that these segments are locked near the surface but creeping at depth. In the first case, a simple elastic dislocation model suggests that the width of the zone of high strain would be roughly equal to the distance from the nearest creeping segment, which is up to 5 km in the center of the North Shore segment. In this area, the zone of high strain rate would be poorly defined and much wider than observed (1–2 km, Figure 6). The data therefore require some amount of creep to be present directly below the North Shore segment, which would be locked only at the surface. In this case, the observed width of the zone of high strain means the locking depth must be small (1–2 km). The top few kilometers of material at North Shore is composed of weak, unconsolidated sediment [*Bilham and Williams*, 1985]. This material is unlikely to support high stresses and should therefore not remain locked for a long period, with creep eventually propagating to the surface. A comparison with ERS data from 1992 to 2007 [*Manzo et al.*, 2011] shows that the broad pattern of deformation at North Shore has been present for at least 20 years and has not become localized during triggered events such as the Landers and Hector Mine earthquakes. We therefore conclude that a purely elastic explanation for the observations is unlikely.

Thanks to high-resolution geodetic methods such as InSAR, distributed creep within fault zones has become detectable only recently. In addition, the signal is subtle (< 20% of the long-term fault slip rate) so that it can currently be observed only on faults with high slip rates. This may help explain the apparent absence of shallow fault creep on a number of lower slip rate faults, despite predictions from laboratory and numerical studies that it should be common [*Dieterich*, 1978; *Ruina*, 1983; *Rice and Ruina*, 1983; *Tse and Rice*, 1986; *Marone and Scholz*, 1988; *Marone et al.*, 1991; *Blanpied et al.*, 1991, 1995; *Scholz*, 1998; *Lapusta et al.*, 2000].

Distributed creep during the interseismic period could also help explain the shallow slip deficit inferred for a number of large ($M \sim 7$) strike-slip earthquakes [*Fialko et al.*, 2005; *Kaneko and Fialko*, 2011; *Wang*, 2013]. *Kaneko and Fialko* [2011] showed that a shallow slip deficit could partially result from off-fault inelastic deformation due to large dynamic stress changes during seismic rupture, but for reasonable values of material cohesion the predicted plastic strain is insufficient to explain the observed slip deficit. *Dolan and Haravitch* [2014] suggested that the amount of shallow slip deficit is inversely correlated with fault age, and therefore may be related to fault complexity.

Finally, distributed interseismic creep may lead to a systematic bias in paleoseismic slip rate estimates, especially if coseismic slip on the respective fault segments is also distributed in a shear zone having a width of a few km. A number of studies seeking to reconcile geodetic and geologic slip rates in California have suggested that between 10% and 30% of the total plate motion may take place as distributed deformation [*Bird*, 2009; *Titus et al.*, 2011; *Johnson*, 2013], with potentially even higher rates in geometrically complex areas such as the Eastern California shear zone [*Herbert et al.*, 2014]. Whether this additional deformation occurs predominantly seismically or aseismically is therefore a critical question for estimates of seismic hazard. Slip on a nonplanar fault can generate dynamic stress concentrations that could locally enhance the occurrence of distributed coseismic yielding [e.g., *Dunham et al.*, 2011], while our results show that geometric complexity can also lead to distributed inelastic deformation during the interseismic period. Future observations will show whether strain localization during seismic events correlates with strain localization in the shallow crust during the interseismic period.

5. Conclusions

We present new geodetic observations from InSAR and GPS of the rate and pattern of shallow creep along the southern San Andreas Fault. The data reveal a systematic variation in the width of the yielding zone. InSAR observations from multiple viewing geometries allow us to resolve horizontal and vertical motions

and provide estimates of the creep rate that are in good agreement with repeated GPS surveys and with creepmeters located along the fault. In areas where the local fault strike results in transpression, creep is localized on a narrow trace (Figure 2b). In the intervening transtensional segments, where fault creep had not previously been detected, we find that fault-parallel shear occurs over a zone approximately 1–2 km wide (Figure 6). The observations also verify ongoing uplift of Durmid Hill at a rate of approximately 1–2 mm/yr, as observed by *Sylvester et al.* [1993] (Figure 2a). Using a simple boundary element model, we show that distributed inelastic yielding can occur in areas where the fault geometry causes stresses to exceed the Mohr-Coulomb failure criterion off the fault plane (Figure 7). If distributed yielding in the interseismic period is common, it may explain the shallow slip deficit in strong ($M \sim 7$) strike-slip earthquakes and may result in a systematic underestimation of the long-term fault slip rates based on paleoseismic data.

References

Allam, A. A., and Y. Ben-Zion (2012), Seismic velocity structures in the southern California plate-boundary environment from double-difference tomography, *Geophys. J. Int.*, *190*(2), 1181–1196, doi:10.1111/j.1365-246X.2012.05544.x.

Allen, C. R., M. Wyss, J. N. Brune, A. Grantz, and R. E. Wallace (1972), Displacements on the Imperial, Superstition Hills, and San Andreas faults triggered by the Borrego Mountain earthquake, *U.S. Geol. Surv. Prof. Pap.*, *787*, 87–104.

Ambraseys, N. (1970), Some characteristic features of the North Anatolian Fault zone, *Tectonophysics*, *9*, 143–165, doi:10.1016/0040-1951(70)90014-4.

Ben-Zion, Y., Z. Peng, D. Okaya, L. Seeber, J. G. Armbruster, N. Ozer, A. J. Michael, S. Baris, and M. Aktar (2003), A shallow fault-zone structure illuminated by trapped waves in the Karadere-Duzce branch of the North Anatolian Fault, western Turkey, *Geophys. J. Int.*, *152*, 699–699, doi:10.1046/j.1365-246X.2003.01870.x.

Berardino, P., G. Fornaro, R. Lanari, and E. Sansosti (2002), A new algorithm for surface deformation monitoring based on small baseline differential SAR interferograms, *IEEE Trans. Geosci. Remote Sens.*, *40*, 2375–2383, doi:10.1109/TGRS.2002.803792.

Bilham, R., and P. Williams (1985), Sawtooth segmentation and deformation processes on the southern San Andreas Fault, California, *Geophys. Res. Lett.*, *12*, 557–560, doi:10.1029/GL012i009p00557.

Bilham, R., N. Suszek, and S. Pinkney (2004), California creepmeters, *Seismol. Res. Lett.*, *75*(4), 481–492, doi:10.1785/gssrl.75.4.481.

Bird, P. (2009), Long-term fault slip rates, distributed deformation rates, and forecast of seismicity in the western United States from joint fitting of community geologic, geodetic, and stress direction data sets, *J. Geophys. Res.*, *114*, B11403, doi:10.1029/2009JB006317.

Blanpied, M., T. Tullis, and J. Weeks (1995), Frictional slip of granite at hydrothermal conditions, *J. Geophys. Res.*, *100*, 13,045–13,064, doi:10.1029/95JB00862.

Blanpied, M. L., D. A. Lockner, and J. D. Byerlee (1991), Fault stability inferred from granite sliding experiments at hydrothermal conditions, *Geophys. Res. Lett.*, *18*(4), 609–612, doi:10.1029/91GL00469.

Bock, Y., R. M. Nikolaidis, and P. J. de Jonge (2000), Instantaneous geodetic positioning at medium distances with the Global Positioning System, *J. Geophys. Res.*, *105*, 28,223–28,253, doi:10.1029/2000JB900268.

Bürgmann, R. (1991), Transpression along the southern San Andreas fault, Durmid Hill, California, *Tectonics*, *10*, 1152–1163, doi:10.1029/91TC01443.

Bürgmann, R., P. Rosen, and E. Fielding (2000a), Synthetic aperture radar interferometry to measure Earth's surface topography and its deformation, *Annu. Rev. Earth Planet. Sci.*, *28*, 169–209, doi:10.1146/annurev.earth.28.1.169.

Bürgmann, R., D. Schmidt, R. Nadeau, M. d'Alessio, E. Fielding, D. Manaker, T. McEvilly, and M. Murray (2000b), Earthquake potential along the northern Hayward Fault, California, *Science*, *289*, 1178–1182, doi:10.1126/science.289.5482.1178.

Cakir, Z., A. M. Akoglu, S. Belabbes, S. Ergintav, and M. Meghraoui (2005), Creeping along the Ismetpasa section of the North Anatolian Fault (western Turkey): Rate and extent from InSAR, *Earth Planet. Sci. Lett.*, *238*(1–2), 225–234, doi:10.1016/j.epsl.2005.06.044.

Cakir, Z., S. Ergintav, H. Ozener, U. Dogan, A. M. Akoglu, M. Meghraoui, and R. Reilinger (2012), Onset of aseismic creep on major strike-slip faults, *Geology*, *40*, 1115–1118, doi:10.1130/G33522.1.

Chen, C. W., and H. A. Zebker (2000), Network approaches to two-dimensional phase unwrapping: Intractability and two new algorithms, *J. Opt. Soc. Am. A*, *17*, 401–414, doi:10.1364/JOSAA.17.000401.

Cochran, E. S., Y.-G. Li, P. M. Shearer, S. Barbot, Y. Fialko, and J. E. Vidale (2009), Seismic and geodetic evidence for extensive, long-lived fault damage zones, *Geology*, *37*, 315–318, doi:10.1130/G25306A.1.

Crouch, S. L., and A. M. Starfield (1983), *Boundary Element Methods in Solid Mechanics*, 322 pp., Allen and Unwin, Boston, Mass.

Crowell, B. W., Y. Bock, D. T. Sandwell, and Y. Fialko (2013), Geodetic investigation into the deformation of the Salton Trough, *J. Geophys. Res. Solid Earth*, *118*, 5030–5039, doi:10.1002/jgrb.50347.

Dieterich, J. H. (1978), Time-dependent friction and the mechanics of stick-slip, *Pure Appl. Geophys.*, *116*, 790–806, doi:10.1007/BF00876539.

Dolan, J. F., and B. D. Haravitch (2014), How well do surface slip measurements track slip at depth in large strike-slip earthquakes? The importance of fault structural maturity in controlling on-fault slip versus off-fault surface deformation, *Earth Planet. Sci. Lett.*, *388*, 38–47, doi:10.1016/j.epsl.2013.11.043.

Dor, O., T. K. Rockwell, and Y. Ben-Zion (2006), Geological observations of damage asymmetry in the structure of the San Jacinto, San Andreas and Punchbowl faults in southern California: A possible indicator for preferred rupture propagation direction, *Pure Appl. Geophys.*, *163*, 301–349, doi:10.1007/s00024-005-0023-9.

Dunham, E. M., D. Belanger, L. Cong, and J. E. Kozdon (2011), Earthquake ruptures with strongly rate-weakening friction and off-fault plasticity, Part 2: Nonplanar faults, *Bull. Seismol. Soc. Am.*, *101*(5), 2308–2322, doi:10.1785/0120100076.

Elliott, J. R., J. Biggs, B. Parsons, and T. J. Wright (2008), Insar slip rate determination on the Altyn Tagh Fault, Northern Tibet, in the presence of topographically correlated atmospheric delays, *Geophys. Res. Lett.*, *35*, L12309, doi:10.1029/2008GL033659.

Faulkner, D. R., T. M. Mitchell, D. Healy, and M. J. Heap (2006), Slip on 'weak' faults by the rotation of regional stress in the fracture damage zone, *Nature*, *444*, 922–925, doi:10.1038/nature05353.

Fialko, Y. (2006), Interseismic strain accumulation and the earthquake potential on the southern San Andreas Fault system, *Nature*, *441*, 968–971, doi:10.1038/nature04797.

Fialko, Y., and E. Tymofyeyeva (2013), Evaluation of atmospheric phase screens by adaptive common-scene stacking of dense InSAR data sets, Abstract G34B-08 paper presented at 2013 Fall Meeting, AGU.

Fialko, Y., D. Sandwell, D. Agnew, M. Simons, P. Shearer, and B. Minster (2002), Deformation on nearby faults induced by the 1999 Hector Mine earthquake, *Science*, *297*, 1858–1862, doi:10.1126/science.1074671.

Fialko, Y., D. Sandwell, M. Simons, and P. Rosen (2005), Three-dimensional deformation caused by the Bam, Iran, earthquake and the origin of shallow slip deficit, *Nature*, *435*, 295–299, doi:10.1038/nature03425.

Fialko, Y. A., and A. M. Rubin (1997), Numerical simulation of high pressure rock tensile fracture experiments: Evidence of an increase in fracture energy with pressure?, *J. Geophys. Res.*, *102*, 5231–5242, doi:10.1029/96JB03859.

Funning, G. J., R. Bürgmann, A. Ferretti, F. Novali, and A. Fumagalli (2007), Creep on the Rodgers Creek Fault, northern San Francisco Bay area from a 10 year PS-InSAR dataset, *Geophys. Res. Lett.*, *34*, L19306, doi:10.1029/2007GL030836.

Genrich, J. F., and Y. Bock (1992), Rapid resolution of crustal motion at short ranges with the Global Positioning System, *J. Geophys. Res.*, *97*(B3), 3261–3269, doi:10.1029/91JB02997.

Genrich, J. F., and Y. Bock (2006), Instantaneous geodetic positioning with 10-50 Hz GPS measurements: Noise characteristics and implications for monitoring networks, *J. Geophys. Res.*, *111*, B03403, doi:10.1029/2005JB003617.

Herbert, J. W., M. L. Cooke, M. Oskin, and O. Difo (2014), How much can off-fault deformation contribute to the slip rate discrepancy within the Eastern California shear zone?, *Geology*, *42*(1), 71–74, doi:10.1130/G34738.1.

Hetland, E. A., P. Musé, M. Simons, Y. N. Lin, P. S. Agram, and C. J. DiCaprio (2012), Multiscale InSAR time series (MInTS) analysis of surface deformation, *J. Geophys. Res.*, *117*, B02404, doi:10.1029/2011JB008731.

Hsu, L., and R. Bürgmann (2006), Surface creep along the Longitudinal Valley Fault, Taiwan from InSAR measurements, *Geophys. Res. Lett.*, *33*, L06312, doi:10.1029/2005GL024624.

Johnson, K. M. (2013), Slip rates and off-fault deformation in Southern California inferred from GPS data and models, *J. Geophys. Res. Solid Earth*, *114*, 5643–5664, doi:10.1002/jgrb.50365.

Jolivet, R., R. Burgmann, and N. Houlie (2009), Geodetic exploration of the elastic properties across and within the northern San Andreas Fault zone, *Earth Planet. Sci. Lett.*, *288*, 126–131, doi:10.1016/j.epsl.2009.09.014.

Jolivet, R., C. Lasserre, M.-P. Doin, S. Guillaso, G. Peltzer, R. Dailu, J. Sun, Z.-K. Shen, and X. Xu (2012), Shallow creep on the Haiyuan Fault (Gansu, China) revealed by SAR interferometry, *J. Geophys. Res.*, *117*, doi:10.1029/2011JB008732.

Jolivet, R., C. Lasserre, M.-P. Doin, G. Peltzer, J.-P. Avouac, J. Sun, and R. Dailu (2013), Spatio-temporal evolution of aseismic slip along the Haiyuan Fault, China: Implications for fault frictional properties, *Earth Planet. Sci. Lett.*, *377–378*, 23–33, doi:10.1016/j.epsl.2013.07.020.

Kaneko, Y., and Y. Fialko (2011), Shallow slip deficit due to large strike-slip earthquakes in dynamic rupture simulations with elasto-plastic off-fault response, *Geophys. J. Int.*, *186*, 1389–1403, doi:10.1111/j.1365-246X.2011.05117.x.

Kaneko, Y., Y. Fialko, D. T. Sandwell, X. Tong, and M. Furuya (2013), Interseismic deformation and creep along the central section of the North Anatolian Fault (Turkey): InSAR observations and implications for rate-and-state friction properties, *J. Geophys. Res. Solid Earth*, *118*, 316–331, doi:10.1029/2012JB009661.

Lapusta, N., J. Rice, Y. Ben-Zion, and G. Zheng (2000), Elastodynamic analysis for slow tectonic loading with spontaneous rupture episodes on faults with rate- and state-dependent friction, *J. Geophys. Res.*, *105*, 23,765–23,789, doi:10.1029/2000JB900250.

Lewis, M. A., Z. Peng, Y. Ben-Zion, and F. L. Vernon (2005), Shallow seismic trapping structure in the San Jacinto Fault zone near Anza, California, *Geophys. J. Int.*, *162*, 867–881, doi:10.1111/j.1365-246X.2005.02684.x.

Lindsey, E. O., and Y. Fialko (2013), Geodetic slip rates in the southern San Andreas Fault system: Effects of elastic heterogeneity and fault geometry, *J. Geophys. Res. Solid Earth*, *118*, 689–697, doi:10.1029/2012JB009358.

Lindsey, E. O., V. J. Sahakian, Y. Fialko, Y. Bock, S. Barbot, and T. K. Rockwell (2013), Interseismic strain localization in the San Jacinto fault zone, *Pure Appl. Geophys.*, 1–18, doi:10.1007/s00024-013-0753-z.

Lockner, D. A., J. Byerlee, V. Kuksenko, A. Ponomarev, and A. Sidorin (1992), Observations of quasistatic fault growth from acoustic emissions, in *Fault Mechanics and Transport Properties of Rocks*, edited by B. Evans and T. Wong, pp. 3–31, Academic Press, San Diego, Calif.

Louie, J. N., C. R. Allen, D. C. Johnson, P. C. Haase, and S. N. Cohn (1985), Fault slip in Southern California, *Bull. Seismol. Soc. Am.*, *75*(3), 811–833.

Lundgren, P. E., A. Hetland, Z. Liu, and E. J. Fielding (2009), Southern San Andreas—San Jacinto Fault system slip rates estimated from earthquake cycle models constrained by GPS and interferometric synthetic aperture radar observations, *J. Geophys. Res.*, *114*, B02403, doi:10.1029/2008JB005996.

Lyons, S., and D. Sandwell (2003), Fault creep along the southern San Andreas from interferometric synthetic aperture radar, permanent scatterers, and stacking, *J. Geophys. Res.*, *108*(B1), 2047, doi:10.1029/2002JB001831.

Lyons, S. N., Y. Bock, and D. T. Sandwell (2002), Creep along the Imperial Fault, Southern California, from GPS measurements, *J. Geophys. Res.*, *107*(B10), 2249, doi:10.1029/2001JB000763.

Manzo, M., Y. Fialko, F. Casu, A. Pepe, and R. Lanari (2011), A quantitative assessment of DInSAR measurements of interseismic deformation: The Southern San Andreas Fault case study, *Pure Appl. Geophys.*, *166*, 1425–1459, doi:10.1007/s00024-011-0403-2.

Marone, C., and C. H. Scholz (1988), The depth of seismic faulting and the upper transition from stable to unstable slip regimes, *Geophys. Res. Lett.*, *15*, 621–624, doi:10.1029/GL015i006p00621.

Marone, C., C. Scholz, and R. Bilham (1991), On the mechanics of earthquake afterslip, *J. Geophys. Res.*, *96*, 8441–8452, doi:10.1029/91JB00275.

McNabb, J. C., and R. J. Dorsey (2012), Stratigraphic record of vertical crustal motions in the past 2-3 ma along the southern San Andreas fault, Mecca Hills, California, Abstract T51B-2582 paper presented at 2012 Fall Meeting, AGU, San Francisco, Calif.

Melin, S. (1986), When does a crack grow under mode II conditions, *Int. J. Fract.*, *30*, 103–114, doi:10.1007/BF00034020.

Neal, R. M. (2003), Slice sampling, *Ann. Stat.*, *31*, 705–767, doi:10.1214/aos/1056562461.

Oskin, M., L. Perg, D. Blumentritt, S. Mukhopadhyay, and A. Iriondo (2007), Slip rate of the Calico Fault: Implications for geologic versus geodetic rate discrepancy in the Eastern California Shear Zone, *J. Geophys. Res.*, *112*, B03402, doi:10.1029/2006JB004451.

Peltzer, G., F. Crampe, S. Hensley, and P. Rosen (2001), Transient strain accumulation and fault interaction in the Eastern California shear zone, *Geology*, *29*, 975–978.

Petit, J.-P., and M. Barquins (1988), Can natural faults propagate under mode II conditions?, *Tectonics*, *7*(6), 1243–1256, doi:10.1029/TC007i006p01243.

Rice, J. R., and A. L. Ruina (1983), Stability of steady frictional slipping, *J. Appl. Mech.*, *50*, 343–349, doi:10.1115/1.3167042.

Rockwell, T. K., S. Lindvall, T. Dawson, R. Langridge, W. Lettis, and Y. Klinger (2002), Lateral offsets on surveyed cultural features resulting from the 1999 Izmit and Düce earthquakes, Turkey, *Bull. Seismol. Soc. Am.*, *92*(1), 79–94, doi:10.1785/0120000809.

Ruina, A. (1983), Slip instability and state variable friction laws, *J. Geophys. Res.*, *88*, 10,359–10,370, doi:10.1029/JB088iB12p10359.

Rymer, M. (2000), Triggered surface slips in the Coachella Valley area associated with the 1992 Joshua Tree and Landers, California, earthquakes, *Bull. Seismol. Soc. Am.*, *90*, 832–848, doi:10.1785/0119980130.

Rymer, M. J., J. Boatwright, L. C. Seekins, J. D. Yule, and J. Liu (2002), Triggered surface slips in the Salton Trough associated with the 1999 Hector Mine, California, earthquake, *Bull. Seismol. Soc. Am.*, *92*, 1300–1317, doi:10.1785/0120000935.

Sandwell, D. T., R. Mellors, X. Tong, M. Wei, and P. Wessel (2011), Open radar interferometry software for mapping surface deformation, *Eos Trans. AGU*, *92*(28), 234, doi:10.1029/2011EO280002.

Savage, J., and M. Lisowski (1993), Inferred depth of creep on the Hayward Fault, Central California, *J. Geophys. Res.*, *98*, 787–793, doi:10.1029/92JB01871.

Scholz, C. H. (1998), Earthquakes and friction laws, *Nature*, *391*, 37–42, doi:10.1038/34097.

Shelef, E., and M. Oskin (2010), Deformation processes adjacent to active faults: Examples from Eastern California, *J. Geophys. Res.*, *115*, B05308, doi:10.1029/2009JB006289.

Shen, Z. K., R. W. King, D. C. Agnew, M. Wang, T. A. Herring, D. Dong, and P. Fang (2011), A unified analysis of crustal motion in Southern California, 1970–2004: The SCEC crustal motion map, *J. Geophys. Res.*, *116*, B11402, doi:10.1029/2011JB008549.

Shirzaei, M., and R. Bürgmann (2013), Time-dependent model of creep on the Hayward Fault from joint inversion of 18 years of InSAR and surface creep data, *J. Geophys. Res. Solid Earth*, *118*, 1733–1746, doi:10.1002/jgrb.50149.

Shirzaei, M., and T. R. Walter (2011), Estimating the effect of satellite orbital error using wavelet-based robust regression applied to InSAR deformation data, *IEEE Trans. Geosci. Remote Sens.*, *49*(11), 4600–4605, doi:10.1109/TGRS.2011.2143419.

Sieh, K., and P. Williams (1990), Behavior of the southernmost San Andreas fault during the past 300 years, *J. Geophys. Res.*, *95*, 6629–6645, doi:10.1029/JB095iB05p06629.

Sieh, K. E. (1982), Slip along the San Andreas Fault associated with the earthquake, *U.S. Geol. Surv. Prof. Pap.*, *1254*, 155–159.

Spudich, P., and K. Olsen (2001), Fault zone amplified waves as a possible seismic hazard along the Calaveras Fault in Central California, *Geophys. Res. Lett.*, *28*, 2533–2536, doi:10.1029/2000GL011902.

Stirling, M. W., S. G. Wesnousky, and K. Shimazaki (1996), Fault trace complexity, cumulative slip, and the shape of the magnitude-frequency distribution for strike-slip faults: A global survey, *Geophys. J. Int.*, *124*, 833–868, doi:10.1111/j.1365-246X.1996.tb05641.x.

Sylvester, A. (1988), Strike-slip faults, *Geol. Soc. Am. Bull.*, *100*, 1666–1703, doi:10.1130/0016-7606(1988)100<1666:SSF>2.3.CO;2.

Sylvester, A., R. Bilham, M. Jackson, and S. Barrientos (1993), Aseismic growth of Durmid Hill: Southeasternmost San Andreas Fault, California, *J. Geophys. Res.*, *98*, 14,233–14,243, doi:10.1029/93JB01028.

Tarantola, A. (2005), *Inverse Problem Theory and Methods for Model Parameter Estimation*, Soc. for Ind. Appl. Math., Philadelphia, Pennsylvania.

Titus, S. J., C. DeMets, and B. Tikoff (2005), New slip rate estimates for the creeping segment of the San Andreas Fault, California, *Geology*, *33*, 205–208, doi:10.1130/G21107.1.

Titus, S. J., M. Dyson, C. DeMets, B. Tikoff, F. Rolandone, and R. Bürgmann (2011), Geologic versus geodetic deformation adjacent to the San Andreas Fault, Central California, *Geol. Soc. Am. Bull.*, *123*(5–6), 794–820, doi:10.1130/B30150.1.

Tong, X., D. T. Sandwell, and B. Smith-Konter (2013), High-resolution interseismic velocity data along the San Andreas Fault from GPS and InSAR, *J. Geophys. Res. Solid Earth*, *118*, 369–389, doi:10.1029/2012JB009442.

Tse, S. T., and J. R. Rice (1986), Crustal earthquake instability in relation to the depth variation of frictional slip properties, *J. Geophys. Res.*, *91*, 9452–9472, doi:10.1029/JB091iB09p09452.

van der Woerd, J., Y. Klinger, K. Sieh, P. Tapponnier, F. Ryerson, and A. Meriaux (2006), Long-term slip rate of the southern San Andreas Fault from ^{10}Be-^{26}Al surface exposure dating of an offset alluvial fan, *J. Geophys. Res.*, *111*, B04407, doi:10.1029/2004JB003559.

Wang, Y. (2013), Earthquake geology of Myanmar, PhD thesis, California Institute of Technology, Pasadena, Calif.

Wechsler, N., T. K. Rockwell, and Y. Ben-Zion (2009), Application of high resolution DEM data to detect rock damage from geomorphic signals along the central San Jacinto Fault, *Geomorphology*, *113*, 82–96, doi:10.1016/j.geomorph.2009.06.007.

Wei, M., D. Sandwell, and Y. Fialko (2009), A silent M4.8 slip event of October 3-6, 2006, on the Superstition Hills fault, Southern California, *J. Geophys. Res.*, *114*, B07402, doi:10.1029/2008JB006135.

Wei, M., D. Sandwell, Y. Fialko, and R. Bilham (2011), Slip on faults in the Imperial Valley triggered by the 4 April 2010 Mw 7.2 El Mayor-Cucapah earthquake revealed by InSAR, *Geophys. Res. Lett.*, *38*, L01308, doi:10.1029/2010GL045235.

Wei, M., Y. Kaneko, Y. Liu, and J. J. McGuire (2013), Episodic fault creep events in California controlled by shallow frictional heterogeneity, *Nat. Geosci.*, *6*, 566–570, doi:10.1038/ngeo1835.

Wesnousky, S. (1988), Seismological and structural evolution of strike-slip faults, *Nature*, *335*, 340–342, doi:10.1038/335340a0.

Wessel, P., W. H. F. Smith, R. Scharroo, J. F. Luis, and F. Wobbe (2013), Generic mapping tools: Improved version released, *Eos Trans. AGU*, *94*, 409–410, doi:10.1002/2013EO450001.